Jianjun He and Weizhou Xiong*

Effect of High Temperature Hot Corrosion on the Compression Creep Behavior of 12Cr1MoV Alloys

DOI 10.1515/htmp-2016-0027
Received February 6, 2016; accepted September 10, 2016

Abstract: This paper highlights the effect of 70 %NaCl–30 %KCl salt mixture on compression creep properties of 12Cr1MoV alloys at 100 MPa (948.15 K, 973.15 K and 998.15 K) in air using bare specimens and specimens in corrosive environment. The corrosive specimens were also tested at 923.15 K (150 MPa, 175 MPa and 200 MPa). Experimental results showed that the specimen in chloride mixture showed relatively high compression creep strain and steady-state creep rates compared with the bare specimen, and this effect accelerated with the increased temperature, especially when it was above 973.15 K. The creep mechanisms of the specimen in chloride mixture were inferred from gliding and climbing of dislocations of the stress exponent. Damage of hot corrosion in creep deformation was found to be associated with the layer fracture attributing to the initiation and propagation from the intergranular cracks and reduction of the bare area caused by the internal transgranular attack of chloride mixture.

Keywords: hot corrosion, compression creep behavior, layer fracture, 12Cr1MoV alloys

Introduction

Most heat tubes in biomass-fired boilers suffer severe damage due to the operational conditions characterized by the following factors: operational environment (high temperature, fuel and air contamination, solid particles etc.) and high mechanical and thermal stresses (due to steam pressure and thermal gradients). Therefore, in these operational conditions, the major degradation factors of tubes in biomass-fired boilers are obviously those mechanical attacks (thermal fatigue and creep attack) and environmental damage (high temperature oxidation, hot corrosion and erosion) which may occur independently or simultaneously [1–3].

Various factors about how hot corrosion lowers the creep life of alloys have been proved by previous studies, such as production of crack on the surface and its propagation [4], reduction of the load bearing on the cross sectional area [5] and defected structures at the grain boundaries by the erosion of molten salt and outward diffusion of metalions [6]. Besides, variation in the salt composition also affects the creep properties of the materials as different salts have different degree of severity to corrode. It has been reported that biomass fuels contain abundant sodium (Na), potassium (K) and chlorine (Cl) which form alkali chloride. The corrosion resulted by alkali chloride is one of the most important factors which should be seriously taken into consideration. Tsaur et al. [7] investigated that the presence of NaCl in-deposit inhibits formation of the protective oxide scale in the initial stage leads to the propagation of hot corrosion on low alloy steels. Depth of the internal attack is deeper with the increase of NaCl in salt mixture. Van lith et al. studied corrosion effects of the alloys in biomass combustion and showed that KCl increase the corrosion rate of materials used as super heater tubes [8]. Some investigations have also proved that mixed chlorides argue for a fast corrosion rate [9–11]. But in actual service conditions, materials will experience both hot corrosion and creep attack and such combined effects have been recently studied. Bagui [12] evaluated the influence of saline environment on creep behaviors of Nimonic-263 and noted that salt mixture extensively affects the creep rupture properties of the material for long duration creep tests. Meanwhile, minimum creep rate increases marginally for the salt deposited sample compared to the bare alloy. Creep behavior of Nimonic-90 under salt-induced high temperature corrosion was evaluated by Gosh [1]. The results indicated that there is an increase in minimum

***Corresponding author: Weizhou Xiong,** School of Power and Energy Engineering, Changsha University of Science and Technology, 960, 2nd Section, Wanjiali South RD, Changsha, Hunan 410114, China, E-mail: 1ansonhiong@126.com
Jianjun He, School of Power and Energy Engineering, Changsha University of Science and Technology, 960, 2nd Section, Wanjiali South RD, Changsha, Hunan 410114, China,
E-mail: 1hejianjun329@126.com

creep rate and a drastic reduction of rupture life in corrosive environment, and he also found that hot corrosion causes severe degradation of materials due to oxidation, sulfidation and chlorination reactions occurring simultaneously.

Since the creep performance has some relationships with the fatigue behavior to some extent, the performance of alloys in hot corrosive environment and under a low cycle fatigue (LCF) load at the same time has attracted great attention and has been valuated recently. Studies illustrated that mechanical properties of alloys, which seriously affect the fatigue behavior, decreased by the salt environment in high temperature [13, 14]. Damage of hot corrosion in fatigue life was found to be associated with the early crack initiation along the weak grain boundaries of recrystallized grains [15].

From the analysis it is pertinent that there exists a wide gap in the area of combined studies relating to hot corrosion and mechanical degradation of alloys, which is essential for design and safety of heat tubes used in the biomass-fired boiler. Most studies currently focus on the tensile creep and low cycle fatigue behaviors of salt-coated alloys used as equipment in power plants. However, as heat tubes are applied in a polytropic stress system so the compression creep behavior of alloys should also be considered. Meanwhile, creep data on 12Cr1MoV in mixed molten chloride is not available in literature. Therefore, it was considered essential to study the behavior of this material under such operating circumstances.

In the present study, the effect of hot corrosion damage on compression creep properties of 12Cr1MoV alloy was investigated at different ranges of temperature (923.15 K–998.15 K) and load stresses (100–200 MPa) in 70 %NaCl–30 %KCl mixture. This study aims (1) to investigate whether the hot corrosion plays a synergic role with the applied stress leading to the progressive loss of material load-bearing capacity in the process of compression creep and (2) to investigate the difference of compression creep deformation between 12Cr1MoV bare specimens and specimens in the hot corrosion environment at different temperatures.

Experimental

Specimen preparations

In this research, the alloy 12Cr1MoV was used after standard treatments, and the solution and aging heat treatment procedures were as follows: 1,453.15 K(2 h) AC + 1,323.15 K(4 h) AC + 1,073.15 K(16 h) AC (AC: air cooling). The chemical compositions (in mass%) of the alloy are given in Table 1. The standard rod specimens with 16 mm height and 9 mm diameter for compression creep tests were machined. All of the specimens were polished using 360, 800, 1,200 SiC sand papers before the test to exclude the surface machining defects.

Table 1: The chemical compositions of the 12Cr1MoV alloy.

Element	C	Si	Cr	Mn	Mo	V
Mass%	0.08–0.15	0.17–0.37	0.90–1.20	0.40–0.70	0.25–0.35	0.15–0.30

The structure of the specimen drawing for the creep test is shown in Figure 1. It was fixed by high temperature inorganic glue in the center of aluminum oxide ceramic tube, the height of which was cut as 12 mm. The tube was also filled with the uniform salt mixture consisting of 70 %NaCl–30 %KCl after solidification of glue for 48 h because 12Cr1MoV alloys suffer from severe corrosion of Cl, Na and K during operation of biomass firing. The salt mixture in each tube is weighted as 1 g.

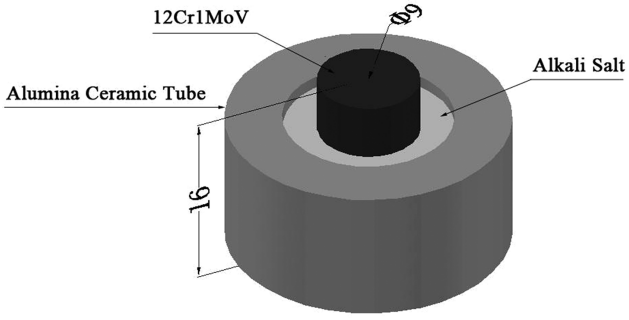

Figure 1: The schematic of the creep testing specimen.

Compression creep tests

High temperature compression creep tests were conducted on a RDL05 electronic creep-fatigue testing machine. Two extensometers were equipped on the machine, both the range of deformation measurement of which is about 5 mm. The heat preservation of specimens was set as 1 h before the test to make specimens under uniform heating. The compression creep tests were conducted at 100 MPa for all the specimens (bare specimens and specimens in salt mixture) at 948.15 K, 973.15 K and 998.15 K. Meanwhile, specimens in hot corrosion environment were also tested at 923.15 K (150 MPa, 175 MPa and 200 MPa). The test matrix is shown in Table 2. The external thermocouples were tied on the specimen for continuous temperature measurement

during the progress of the test and variation of temperature was kept as ± 274.15 K.

Table 2: Compression creep test matrix of the 12Cr1MoV alloy.

Item	Specimens	
	Bare	Corrosive
Stress (MPa)	100	100, 150, 175, 200
Temperature (K)	948.15, 973.15, 998.15	923.15, 948.15, 973.15, 998.15
Salt mixture	70 %NaCl–30 %KCl	70 %NaCl–30 %KCl

Measurements and observations

The surface condition, cross sections, substrate and defected structures were observed using scanning electron microscope (SEM) and energy dispersive spectroscopy (EDS) to investigate the effect of hot corrosion on the compression creep behavior of 12Cr1MoV alloys. Specimens for SEM observations of cross sectional areas were firstly sealed in epoxy resin and mechanically polished. The substrate of alloys were also polished and then cleaned with ethanol and finally etched with mixed 4 % nitric acid and 96 % ethanol for 12–15 s.

Results

Compression creep curves

The creep curves for the compression creep tests conducted at 100 MPa (948.15 K, 973.15 K, 998.15 K) in air on bare specimens and specimens in salt mixture are shown in Figure 2. There exists evident creep deformation both in bare and corrosive specimens, increasing with the ascending temperature. It can also be observed that the strain responses of the corrosive specimens are higher than that of the bare specimens among all values of temperature. Even if the strain variations of specimens in the initial period in different operational environment are similar, there is a strain raise observed at the specimens in hot corrosion environment. Steady-state creep rates of bare specimens and specimens in salt mixtures at different temperature are shown in Table 3, where all the values of corrosive specimens are higher than that of the bare specimens, particularly, when the temperature is above 973.15 K.

Figure 3(a) shows the creep curves of specimens in hot corrosive environment with different applied stresses

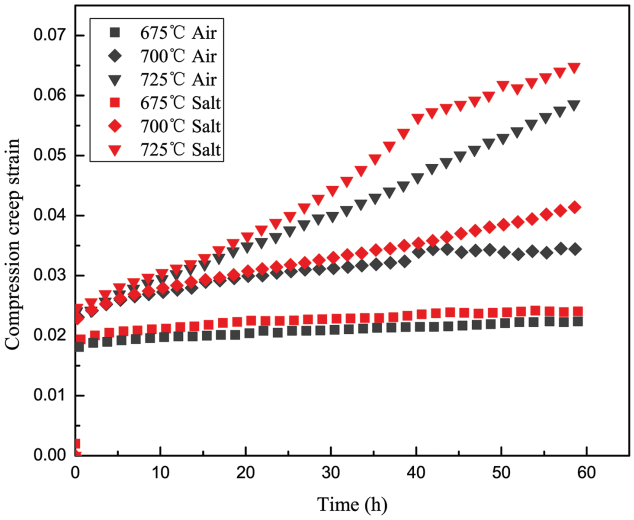

Figure 2: Compression creep curves of bare specimens and specimens in hot corrosive environment at different temperatures.

Table 3: Steady-state creep rates of bare and corrosive specimens at different temperature.

Temperature/K	Stress/MPa	Steady-state creep rate $\dot{\varepsilon}$/mm · S^{-1}	
		Bare	Corrosive
948.15	100	6.641×10^{-5}	6.899×10^{-5}
973.15	100	1.773×10^{-4}	2.462×10^{-4}
998.15	100	5.617×10^{-4}	7.8824×10^{-4}

(150 MPa, 175 MPa and 200 MPa) at 923.15 K. Significantly, there is an increase on the compression creep strain and secondary creep rates (Table 4) with the increasing stresses. It has been proved that creep properties of the alloy are usually characterized by the steady creep rate (minimum creep rate) $\dot{\varepsilon}$ which has a close relationship with self-characteristics of materials and external load σ. Usually the dependence of a minimum creep rate on an applied stress is described by the Norton equation as follows:

$$\dot{\varepsilon} = A\sigma^n \exp(-Q/RT) \quad (1)$$

where $\dot{\varepsilon}$ is the minimum or steady-state creep rate, A is the dimensionless constant factor depending on the material, n is the stress exponent for creep, Q is the activation energy for creep, R is the gas constant, and T is the absolute temperature. Relative researches have proved that there is a linear relationship between ln σ and ln $\dot{\varepsilon}$ from eqs (2) and (3) after taking logarithm on eq. (1). The slope of a plot of ln$\dot{\varepsilon}$, against lnσ is evaluated as the stress exponent n.

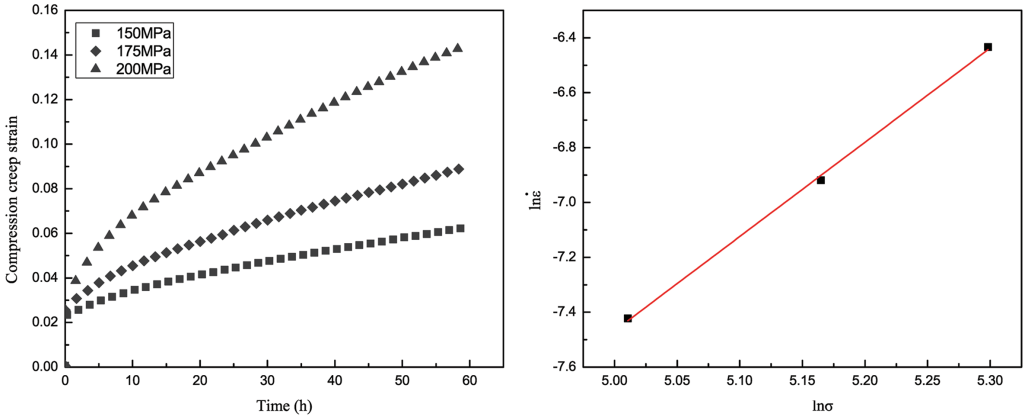

Figure 3: (a) Compression creep curves and (b) the relationship of steady-state creep rates with applied stresses of specimens in hot corrosive environment.

Table 4: Steady-state creep rates of corrosive specimens at different applied stresses.

Applied stress/MPa	Temperature/K	Steady-state creep rate $\dot{\varepsilon}$/mm · S^{-1}
		Corrosive
150	923.15	5.975×10^{-4}
175	923.15	9.888×10^{-4}
200	923.15	1.610×10^{-3}

$$\ln\dot{\varepsilon} = -Q/RT + \ln A + n\ln\sigma \quad (2)$$

$$\ln\dot{\varepsilon} = C' + n\ln\sigma \quad (3)$$

Plots for creep tests performed at 923.15 K are shown in Figure 3(b). The value of the stress exponent is calculated as 3.5. It has been proved that the stress exponent n is directly related to deformation mechanisms taking place during compression creep. A value of $n = 1$ is connected to diffusion deformation mechanisms. A value $n = 3$ is related to viscous glide of dislocations. $n = 5$ is related to dislocation climbing at high temperature and $n = 7$ to dislocation climbing at low temperature [16]. The stress exponent in this test is found to be suitable for determination of mechanisms which occur during creep. According to the value of $n = 3.5$, gliding and climbing of dislocations are the predominant deformation mechanisms of 12Cr1MoV in high temperature chloride mixture condition.

Surface and layers characterization

The high temperature hot corrosion morphology of the specimen in salt mixture was observed after the compression creep test at 948.15 K. The surface of the specimen after chloride corrosion showed a black and dark red appearance because of the existence of corrosive products. The high magnification view of the surface of specimen in salt obtained by SEM is shown in Figure 4 (a)–(b). The surface was observed very rough with clear cracks and abundant porous products. The composition of the corrosive products near the crack was analyzed using EDS as shown in Figure 4(c) and Table 5. Only iron, oxygen, and little carbon were detected, while the chromium and silicon content, as shown in Table 5, both of which existed in the initial state (Table 1) were not detected. This observation indicates that the protective chromium or silicon oxide layer formed and then subsequently broke by hot corrosion damage. In the hot corrosion environment, the protective oxide layer cannot form on the surface of the specimen [15]. Ishitsuka and Nose [17] also noted that the protective Cr_2O_3 scale can be easily dissolved to CrO_4^{2-} in alkali chloride mixture, leading to accelerated corrosion. Thus, hot corrosion is more detrimental than oxidation for alloys at elevated temperature, especially for those in molten NaCl-KCl mixture [18]. According to the appearance of corrosive products and the results of EDS, the products mainly consist of Fe_2O_3 and Fe_3O_4.

The cross sections of the bare compression creep specimens and specimens in chloride mixture observed with SEM at different temperature, contrastively, are shown in Figure 5. In corrosive specimens, cross sections are divided into four layers by the cracks in the direction of the compression stress. The two outer porous layers are surface oxides, whereas the layer separating the inner corrosion layer from the unaffected zone is the transitional corrosion layer. The formed corrosion products were very porous and loosely attached to the substrate. In bare specimens, only outer oxidation and inner oxidation layers were observed. It could be observed that in salt mixture the cracks seriously expands on every layers, accelerating the spalling of the corrosive product and

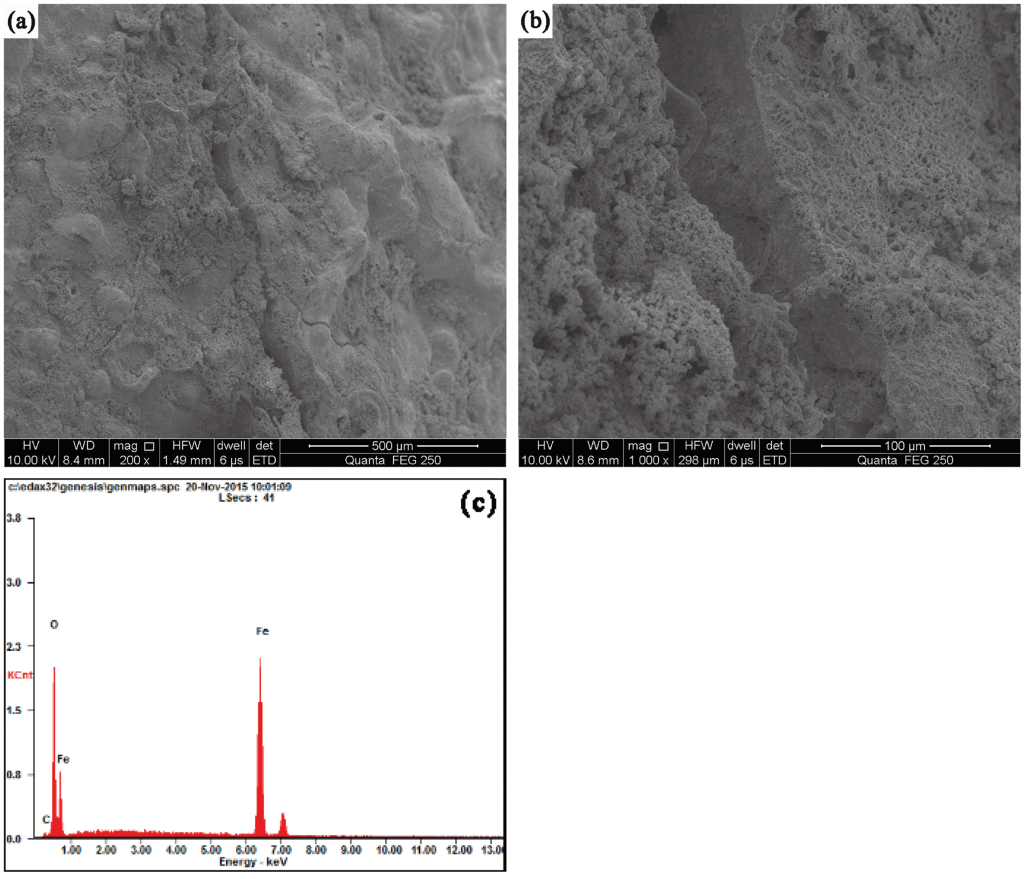

Figure 4: SEM micrograph showing the (a) corrosive surface and the (c) EDS analysis of distinct areas: (b) products near the crack of the corrosive specimen at 948.15 K/100 MPa.

Table 5: Element content of the corrosive products on the surface (948.15 K/100 MPa).

Element	Corrosive surface	At. %
	Mass%	
C	01.74	05.20
O	19.71	44.27
Fe	78.55	50.53

gravely increasing the depth of the oxidation effect when comparing with Figure 5(a) and 5(c) (Figure 5(b) and 5(d)). Meanwhile, the increasing temperature also aggravates the separation of oxidation layers both in bare and corrosive specimens. For example: as it is shown in Figure 5(b), the cross section at a higher temperature has suffered more severe corrosion attack, an increasing thickness of the corrosion area and a wide reduction on the inner corrosion layer were compared in Figure 5(a). While in Figure 5(d), evident fracture among each layers (layer fracture phenomenon) were observed when compared with that in Figure 5(c).

An EDS is used to analyze the chemical compositions on each layers of bare and corrosive specimens at 998.15 K, as it is shown in Figures 6 and 7. Tables 6 and 7 contain composition, including weight and atomic percentages, of the major elements in each of these layers. Several conclusions can be inferred from the measurements of composition and their variations with the depth from external surface. As it can be concluded in Figure 6, the compositions on each corrosion layers are different. The outer layer only exhibits a composite of Fe and O, whereas a composite of matrix and oxidized material were observed from the inner corrosion layer to the unaffected zone. The Cr and Si contents can not be detected in the outer and inner layers, which again prove that protective Cr and Si oxide layers are totally broken by hot corrosion. The content of Cl was detected in the inner corrosion layer and transitional layer. Many of our observations and results of composition indicate that the main corrosion mechanism on cross sections is active oxidation. In details, the structures of formed corrosion product, especially those are shown in Figure 5(b), are similar to the findings described by Metsäjoki et al. [19] and Zahs et al. [20]: layered, porous, cracked and hollow shaped. The detailed mechanism was summarized by Grabke et al. [21] as follows in Reactions (1)–(5), (M = Na, K):

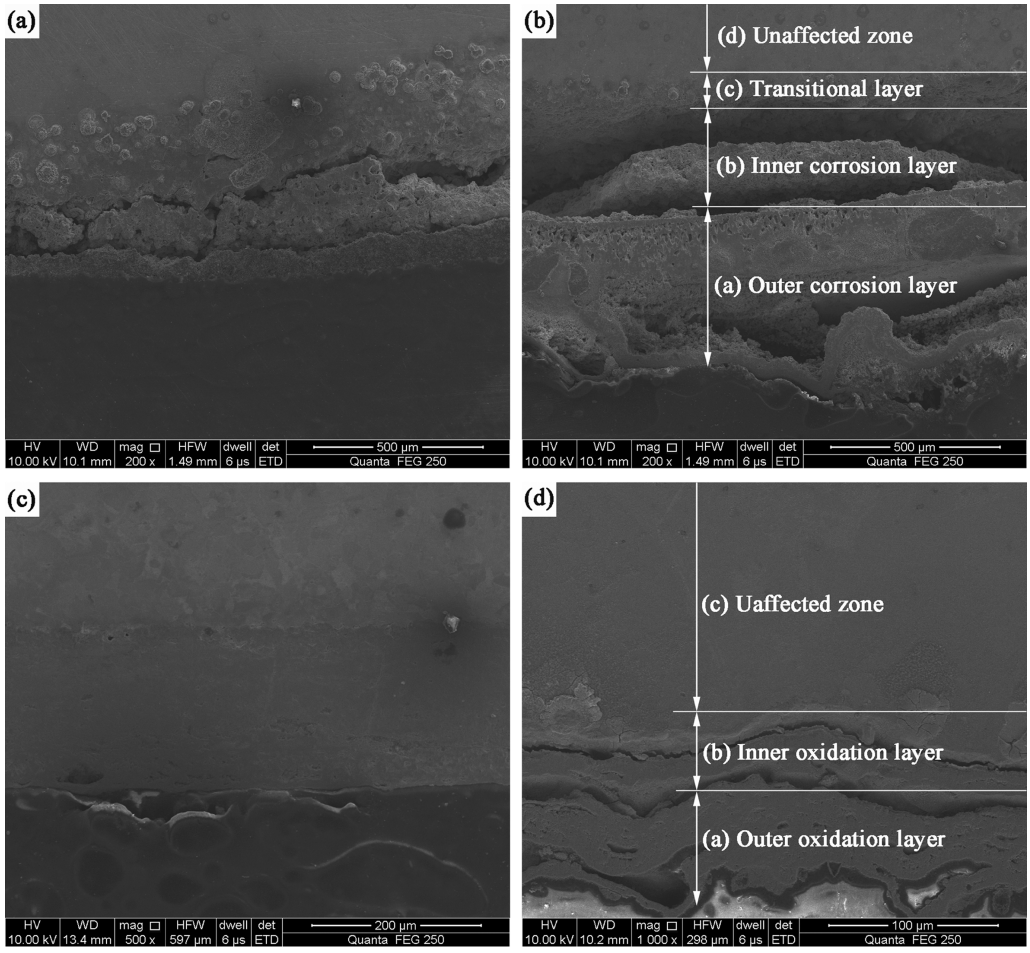

Figure 5: SEM micrograph of the cross sections of corrosive specimens at (a) 973.15 K/100 MPa, (b) 998.15 K/100 MPa and bare specimens at (c) 973.15 K/100 MPa, (d) 998.15 K/100 MPa.

$$2MCl + Fe_2O_3 + 1/2O_2 \leftrightarrow M_2Fe_2O_4 + Cl_2 \quad (1)$$

$$4NaCl + Cr_2O_3 + 5/2O_2 \leftrightarrow 2NaCrO_4 + 2Cl_2 \quad (2)$$

$$Fe + Cl_2 \leftrightarrow FeCl_2 \quad (3)$$

$$2FeCl_2 + 3/2O_2 \leftrightarrow Fe_2O_3 + 2Cl_2 \quad (4)$$

$$3FeCl_2 + 2O_2 \leftrightarrow Fe_3O_4 + 3Cl_2 \quad (5)$$

Antunes et al. [3] had noted that the active oxidation occurs when the oxide scale on the metallic surface has no protective character and chloride based contaminants strongly accelerate its oxidation rate. From those reactions and EDS results, it is can be seen that the outer layer consists of a porous Fe_2O_3/Fe_3O_4. The inner layer is an oxide which is composed of $Fe_2O_3/Fe_3O_4/FeCl_2$, while $Fe_2O_3/Fe_3O_4/Cr_2O_3/FeCl_2$ are the main compositions on transitional layers. In Figure 7, as there is only hot oxidation on the cross section of the bare specimen, the major components are nearly the same in outer and inner oxidation layers, which are Fe_2O_3 and Cr_2O_3. The average and maximal thickness of both oxide layers of corrosive specimens were higher than the corresponding values for bare specimens. The depth of the corrosion affected area is approximately 1 mm in Figure 5(b). However, the thickness of bare layers of the same alloy in Figure 5(d) is only about 100 μm. This mainly attributed to the fact that the cycles of reactions (3)–(6) of the specimen in chloride can be repeated, sustaining the oxidation of the metallic surface beneath the non-protective oxide scale.

The surface microstructure of the transitional area after removing of the inner fracture layer of the specimen at 998.15 K (sub-surface) is shown in Figure 8. This surface is the result of fissure between the inner corrosion layer and transitional layer, which illustrate the crack propagation mechanism among each layer. Figure 8(a) shows the corrosion morphology of the sub-surface where the corrosion mechanism of chloride mixture was observed as intergranular attack. The effect is uneven for the reason that a part of grain boundaries are slightly

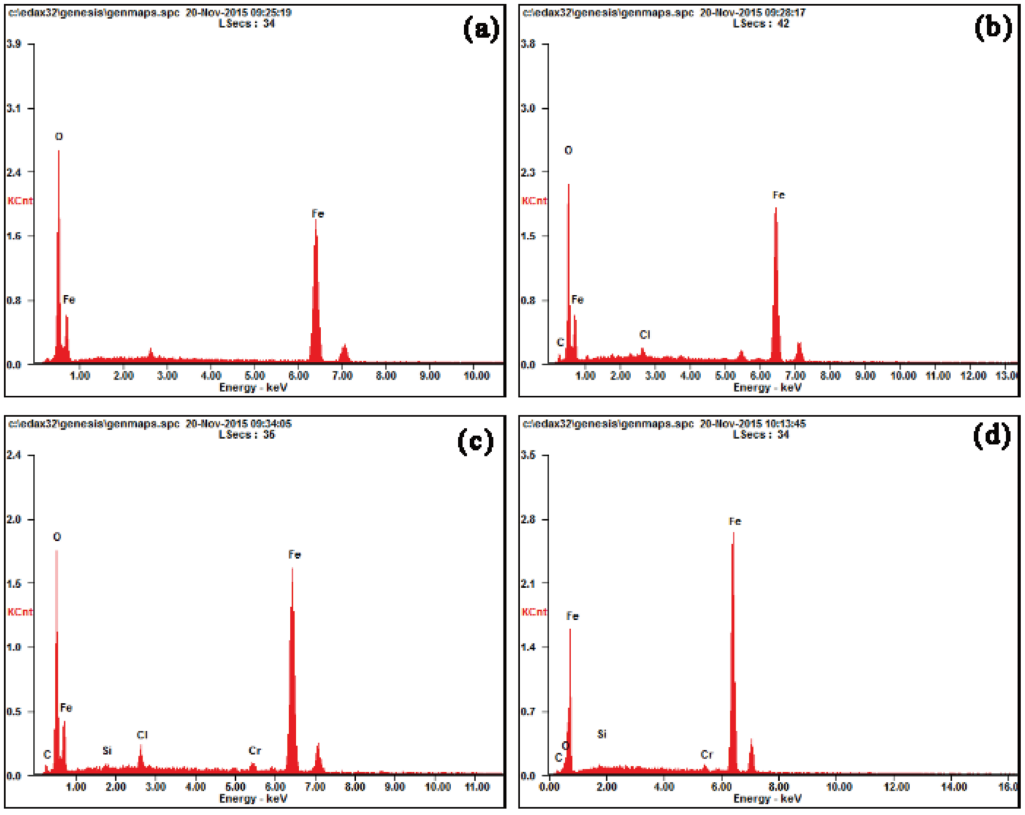

Figure 6: Spectrum for the (a) outer corrosion layer, (b) inner corrosion layer, (c) transitional layer and (d) unaffected zone of the corrosive specimen at 998.15 K/100 MPa.

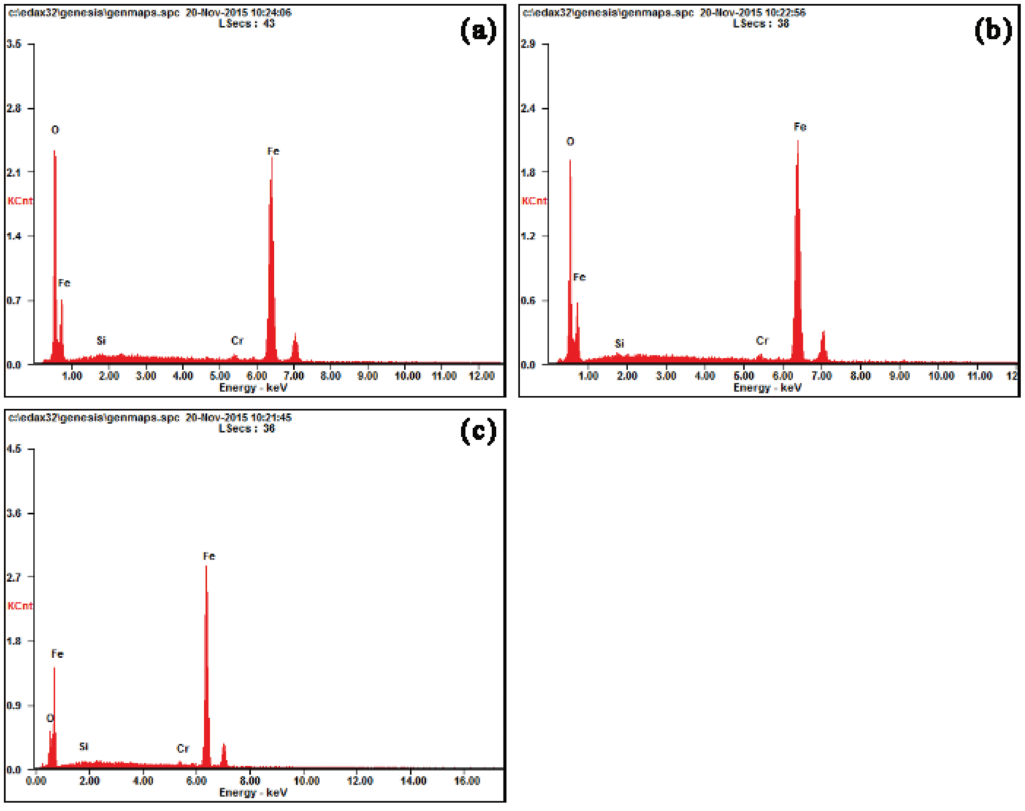

Figure 7: Spectrum for the (a) outer oxidation layer, (b) inner oxidation layer and (c) unaffected zone of the bare specimen at 998.15 K/100 MPa.

Table 6: Composition of cross-sectional layers on the corrosive specimen (998.15 K/100 MPa).

Element	Outer corrosion layer		Inner corrosion layer		Transitional layer		Unaffected zone	
	Mass%	At. %	Mass%	At. %	Mass%	At. %	Mass%	At. %
Fe	74.54	45.62	72.78	42.89	73.24	45.76	95.69	87.84
O	25.46	54.38	22.55	46.37	19.61	42.77	01.24	03.98
C	–	–	03.53	09.68	02.54	07.38	01.48	06.30
Cl	–	–	01.14	01.06	02.17	02.14	–	–
Si	–	–	–	–	00.55	00.68	00.37	00.68
Cr	–	–	–	–	01.89	01.27	01.22	01.20

Table 7: Composition of cross-sectional layers on the bare specimen (998.15 K/100 MPa).

Element	Outer oxidation layer		Inner oxidation layer		Unaffected zone	
	Mass%	At. %	Mass%	At. %	Mass%	At. %
Fe	78.46	52.24	81.30	56.66	94.40	85.44
O	19.95	46.36	17.30	42.08	04.01	12.66
Si	00.43	00.57	00.34	00.47	00.42	00.75
Cr	01.17	00.83	01.06	00.79	01.18	01.15

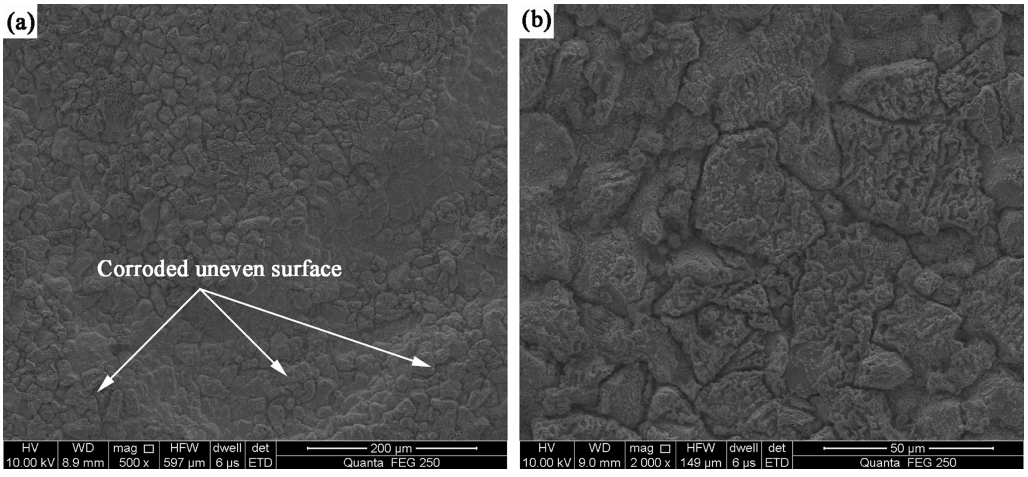

Figure 8: SEM micrograph of the (a) surface of transitional areas and (b) the amplification of grains and grain boundaries at 998.15 K/100 MPa.

corroded, which is concerning with the applied stress to some extent. The detailed characterization on the local area of secondary surface is shown in Figure 8(b). Both the grains and grain boundaries were observed under severe attack. The grains are covered by abundant fold-like corrosive products on which some transgranular cracks were observed.

The representative micrographs of transitional layers of the corrosive and bare specimens are shown in Figure 9. A distinct comparison of cracks between the affected area and substrate was observed. For the corrosive specimen, as shown in Figure 9(a), intergranular cracking was revealed, which is similar to the morphology of the sub-surface in Figure 8(a). As in high temperature environment, the atomic arrangement of grain boundaries is irregular and atoms of grain boundaries are more active than that in grains, leading to a rapid drop of strength on grain boundaries. Crack initiation easily occurs in this area because effects of adhesion among grains weakened by hot corrosion. Meanwhile, glide caused by the applied stress also accelerates the degradation of adhesion and finally results in the

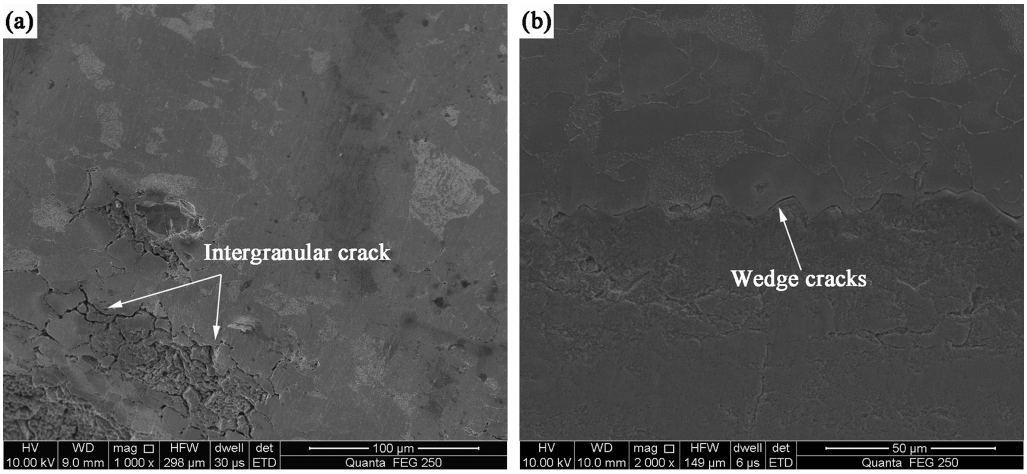

Figure 9: SEM micrograph of cracks and defected structures between the corrosive/oxide layer and unaffected zone of the (a) corrosive specimen and (b) bare specimen at 973.15 K/100 MPa.

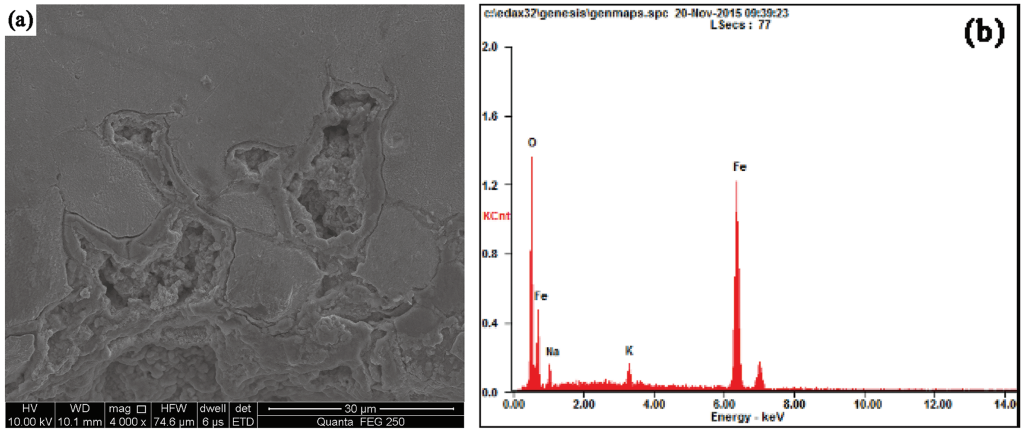

Figure 10: Micrograph of the detailed morphology on (a) corroded grains and the (b) EDS analysis on grain boundaries at 973.15 K/100 MPa.

appearance of intergranular cracks. The oxide layer in salt mixture is uneven, whereas that of the bare specimen is relative flat. After the compression creep test at 973.15 K, serious internal corrosion and spalling were observed at center of grains (Figure 10), where holes and voids with large sizes were exposed. This is the reason why the corrosion layers in Figure 5(a) and 5(b) are loosely and bubbly shaped. The stress concentration due to those defects at high temperature results in transcrystalline cracks initiation on sub-surface and its accelerated growth, which has been observed before in Figure 8(b). However, the corrosion product near grain boundaries is compact and the corrosion effect is slighter, which might attribute to the protection effect of carbide precipitation on the grain boundaries in Figure 11(b). From the EDS analysis in Figure 11(d) and Table 9, the precipitation is mainly composed by Fe, C and Cr, while it could be hardly observed on the received specimen (see Figure 11(a)). The protective chromium oxide degrades the attack of corrosion on grain boundaries. When the working temperature increased during a long term, some rod-like particles on pearlite matrix disappeared gradually and the precipitates became fine and dispersed as shown in Figure 11(c). SEM observations also showed the growth of precipitates and coarsening of particles on the grain boundaries. Furthermore, some fine particles can be found on the ferrite matrix. The result is similar to the findings by Li [22], illustrating that $M_{23}C_6$ is the precipitate production of long-term tempering.

An EDS is used to analyze the chemical composition of the products near grain boundaries as it is shown in Figure 10(b) and Table 8, the Na and K contents are composed, indicating that the mechanism is mainly based on Reactions (1)–(2) and (6). The generated Na_2CrO_4 and K_2CrO_4 is then broken by hot damage, causing the Cr content dissolve into the chloride mixture.

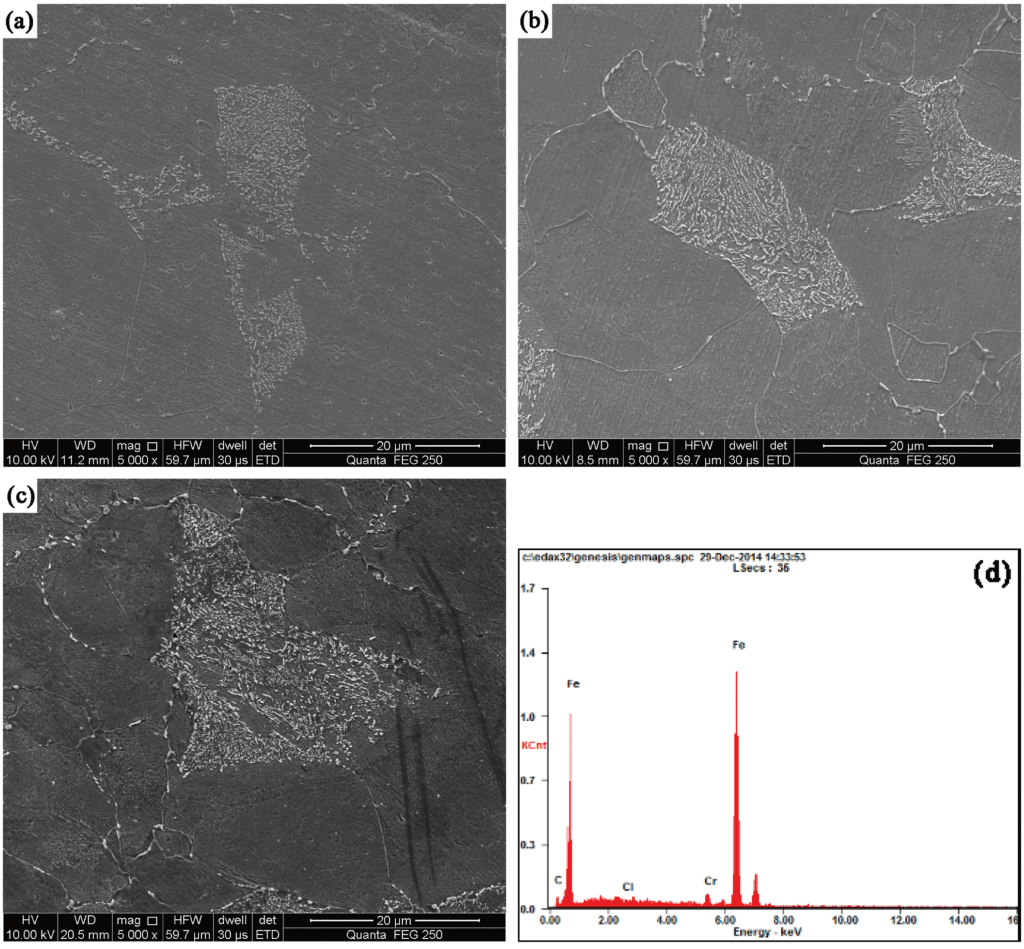

Figure 11: SEM micrograph showing precipitation on substrate areas of the (a) as-received specimen, (b) corrosive specimen at 973.15 K/100 MPa and the (d) spectrum for the precipitation on the grain boundaries of the (c) corrosive specimen at 998.15 K/100 MPa.

Table 8: Composition of grain boundaries in the transitional area of the corrosive specimen (973.15 K/100 MPa).

	Grain boundaries	
Element	**Mass%**	**At. %**
Fe	72.69	45.67
O	20.97	46.00
Na	04.20	06.40
K	02.14	01.92

Table 9: Composition of precipitation on the substrate of the corrosive specimen (998.15 K/100 MPa).

	Grain boundaries	
Element	**Mass%**	**At. %**
Fe	91.85	77.21
C	05.11	19.97
Cr	02.86	02.58
Cl	00.18	00.24

$$2Cr_2O_3 + 8KCl + 5O_2 \leftrightarrow 4K_2CrO_4 + 4Cl_2 \quad (9)$$

By contrast, the bare sample of the same alloy did not reveal interganular cracking. The grains of the bare specimen are compact without spalling of the oxide products. The wedge cracks were observed as an irregular transgranular attack in the direction of stress, resulting in a holistic separation of the inner oxidation layer from the substrate. Such cracks were also observed between the outer oxide layer and inner layer as shown in Figure 5(c).

4 Discussion

In the present study, the compression creep curves were obtained in bare and corrosive specimens and there are some observable effects of high temperature hot corrosion on the creep strain responses. It was observed that initial portions of compression creep curves on bare and corrosive specimens are almost the same approximately up to 10 h (Figure 2). This can mainly attribute to the fact

that hot corrosion initially does not affect the surface condition of the specimen to that extent. The strength of the whole specimen is not degraded by the shallow corrosive products. Similar observation was also made by earlier authors, who noted that the creep rupture life of alloy is not much affected by the corrosive action of the salt mixture for short duration tests [12]. After a certain period of time, the increase of strain response and creep rates were observed because of the strong oxidation and corrosive effects of the salt deposition works in the later stage. The relative study of Guo and his co-workers also showed that the increase of $\dot{\varepsilon}_{min}$is caused by hot corrosion salt-coating, while it does not change the creep mechanism [23]. Therefore, the high temperature hot corrosion damage process is time dependent and the sufficient time given to degrade the creep resistance of structural alloy. Moreover, a higher strain response and creep rate which indicating a more severe corrosion impact is seen for the tests with those at high testing temperature. One possible reason to this behavior is that the active oxidation effect of chloride mixture is aggravated by the increasing temperature, thus leads to faster crack propagation and spalling of the corrosion products on sectional areas. There is an obvious increase of the products among each layer, where the specimen is easier to be deformed. Thus the ascending temperature is also concerning with the effect of hot corrosion on compression creep properties of 12Cr1MoV alloys.

The corrosion and oxidation of the chloride mixture, which work in the later stage create the evident corrosion cracks (see Figure 4) on the surface and is well established by Lin et al. [4] and Bagui et al. [12]. Initiation and propagation of such cracks act as notch introducing triaxiality of stress and are hence stress raisers. The corrosive effect also creates corroded uneven sub-surface as shown in Figure 8. Such surface on the corrosive specimen degrades effective cross sectional area for load bearing capacity of the specimen than that of bare specimen. The layer fracture was observed on the cross section of the bare specimen at 998.15 K (see Figure 5(d)), which is caused by the wedge cracks expand along the borderline of two different layers for a long duration. While the testing temperature is lower than 998.15 K, the fracture can not be evidently observed on the bare specimen. However, hot corrosion extensively accelerates the separation of layers even when the temperature is 973.15 K and the reduction of the bare area on the cross section was also observed by hot corrosion attack. As a result, a higher strain response and minimum creep rate can be found in the secondary creep region of corrosive specimens than in bare specimens at same temperature.

It has been proved that the impact toughness of the Cr-Mo steel is strongly dependent on the precipitates [24]. With the increasing temperature, the microstructures of particles on pearlite matrix and grain boundaries were observed (see Figure 11(b)–11(c)). The decrease of the amount of particles on pearlite has been proved to soften the strength of materials. Precipitation and coarsening of $M_{23}C_6$ at ferrite grain boundaries also result in a sharp deterioration of impact toughness and mechanical properties. Meanwhile, the decrease of the amount of carbon and matrix solubility solid solution due to the precipitation of $M_{23}C_6$ becomes the main softening mechanism of steels [22]. According to those factors, 12Cr1MoV alloys are easier deformed at high temperature, both in corrosive and bare specimens.

Based on the present investigation, the high temperature chloride mixture has been proved to lead to a different crack initiation mechanism and deformation mode when compared with the corrosive and bare specimens. The crack nucleation site of the bare 12Cr1MoV alloy is developed as a result of internal defects by the combined effects of hot oxidation and a compression stress. While for the specimen in high temperature hot corrosion environment, the damage changes surface of the specimen. Therefore, the corrosive specimen is surface-initiated. During the initial state of high temperature hot corrosion on a corrosive specimen, the alloy forms a protective Cr_2O_3 layer [25]. Under a compression loading, the protective oxide layer of Cr_2O_3, forming at the crack front, could be ineffective because of the combined detrimental effects of a load stress and chemical actions of the salt. The previous investigations showed that chloride salt prevent formation of protective scale in the initial stage and induce internal attack [14]. The deleterious effect of chloride mixture attributed to extremely small size of Cl^- ions. The damage caused by chlorine was from self-sustained chlorination and oxidation with metallic ingredients. Cl^- ions quickly penetrate through fluxing holes as well as the grain boundaries and react with internal metallic ingredients to form volatile chromium chloride as shown in Reactions (7)–(10) [26].

$$2Fe_2O_3(s) + 6Cl_2(g) = 4FeCl_3(g) + 3O_2 \quad (7)$$

$$2Cr_2O_3(s) + 6Cl_2(g) = 4CrCl_3(g) + 3O_2(g) \quad (8)$$

$$Fe(s) + 1/2Cl_2 = FeCl_3(g) \quad (9)$$

$$Cr(s) + 1/2Cl_2 = CrCl_3(g) \quad (10)$$

The volatile species thus produced tend to migrate out of the grain boundaries to the surface and in this process they generate numerous pits and voids at the grain

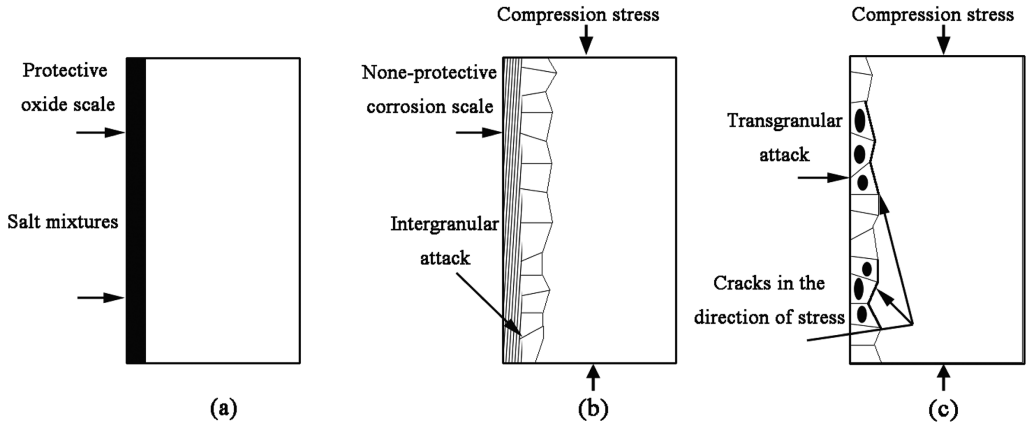

Figure 12: A schematic illustration based on present findings showing the process of compression creep cracks initiation and growth in the 12Cr1MoV alloy in hot corrosion environment.

boundaries. The formation and growth of those cavities result in the intergranular attack. As Cl_2 is reproduced by the active oxidation and repeatedly cause corrosion, penetrating the substrate, those cracks are also initiated on the internal area (see Figures 8 and 9) for the reason that the oxidized grain boundaries are apparently weakened and possess low strength at high temperature. When the compression load is sufficiently high for a long duration, the surface and cross sections break preferably along those intergranular cracks in the direction of the compression stress, result the evident layer fracture on corrosive specimens. Meanwhile, the chloride also subsequently induce the transgranualr attack near those layers (see Figure 10), resulting in the reduction of loose products on the cross section. A schematic mechanism of compression creep crack initiation and growth in the hot chloride condition is shown in Figure 12.

Conclusions

The aforesaid study leads to the following conclusions:

1. High temperature hot corrosion by chloride mixture result in a decrease of the compression creep properties, compared with similar tests for bare specimens. The total creep strain and minimum creep rate of corrosive specimens are all higher than that of bare specimens. The creep mechanisms of specimens in hot chloride mixture are inferred from gliding and climbing of dislocations of the stress exponent. The corrosive effect accelerates as the temperature increases, especially when it is above 973.15 K.
2. 70 %NaCl–30 %KCl mixture causes intergranular cracks and transgranular attack on the specimen. Compression creep cracks in the corrosive specimens are initiated and propagated mostly from the intergranular attack along the direction of stress on the surface and sections. While the cracks in bare specimens are developed as a result of internal defects.
3. Damage of hot corrosion on creep deformation is found to be associated with the reduction of the bare area caused by the internal transgranular attack from the chloride mixture. The layer fracture which is caused by the propagation of creep cracks in corrosive specimens, including outer layer, inner layer and transitional layer degrade the mechanical properties for the alloys.
4. Decrease of the toughness of specimens partly attributed to the disappearance of particles on pearlite, precipitation at ferrite grain boundaries and the coarsening of $M_{23}C_6$ precipitates in high temperature environment.

Funding: The authors are thankful to the National Natural Science Foundation of China (51275058) and College Innovation Platform Project of Hunan Province (13K052) for the support given to this research.

References

[1] K.S. Ghosh, Ind. J. Eng. Mater. sci., 7 (2000) 69–76.
[2] T. Gruber, T.,K. Schulze, R. Scharler I. Obernberger, Fuel, 144 (2015) 15–24.
[3] R.A. Antunes and M.C.L. de Oliveira, Corros. Sci., 76 (2013) 6–26.
[4] T.L. Lin, Y.H. Zhang and H.W. Yang, Mater. Sci. Eng., 62 (1984) 17–24.
[5] V. Suryanarayanan, K.J.L. Iyer and V.M. Radhakrishnan, Mater. Sci. Eng. A, 112 (1989) 107–116.

[6] P. Kofstad, Proceedings of the Symposium on High Temperature Corrosion in Coal Gasification Atmosphere, Elsevier, London (1984), p. 207.
[7] C.C. Tsaur, J.C. Rock, C.J. Wang and Y.H. Su, Mater. Chem. Phys., 89 (2005) 445–453.
[8] S.C. van Lith, F.J. Frandsen, M. Montgomery, T. Vilhelmsen and S.A. Jensen, Energ. Fuel, 23 (2009) 3457–3468.
[9] S.N. Liu, Z.D. Liu, Y.T. Wang and J. Tang, Corros. Sci., 83 (2014) 396–408.
[10] B.P. Mohanty and D.A. Shores, Corros. Sci., 46 (2004) 2893–2907.
[11] D.A. Shores and B.P. Mohanty, Corros. Sci., 46 (2004) 2909–2924.
[12] S. Bagui, A.K. Ray, J.K. Sahu, N. Parida, J. Swaminathan, M. Tamilselvi and S.L. Mannan, Mater. Sci. Eng. A, 566 (2013) 54–60.
[13] J.K. Sahu, R.K. Gupta, J. Swaminathan, N. Paulose and S.L. Mannan, Int. J. Fatigue, 51 (2013) 68–73.
[14] G.S. Mahobia, N. Paulose, S.L. Mannan, R.G. Sudhakar, K. Chattopadhyay, N.C.S. Srinivas and V. Sing, Int. J. Fatigue, 59 (2014) 272–281.
[15] X.G. Yang, S.L. Li and H.Y. Qi, Int. J. Fatigue, 70 (2015) 106–113.
[16] H. Dieringa, N. Hort and K.U. Kainer, Mater. Sci. Eng. A, 510–511 (2009) 382–386.
[17] T. Ishitsuka and K. Nose, Corros. Sci., 44 (2002) 247–263.
[18] M. Broström, S. Enestam, R. Backman and K. Mäkelä, Fuel Process. Technol., 105 (2013) 142–148.
[19] J. Metsäjoki, E. Huttunen-Saarivirta and T. Lepistö, Fuel, 133 (2014) 173–181.
[20] A. Zahs, M. Spiegel and H.J. Grabke, Mater. Corros., 50 (1999) 561–578.
[21] H.J. Grabke, E. Reese and M. Spiegel, Corros. Sci., 37 (1995) 1023–1043.
[22] Z.J. Li, N.M. Xiao, D.Z. Li, J.Y. Zhang, Y.J. Luo and R.X. Zhang, Mater. Sci. Eng. A, 604 (2014) 103–110.
[23] J.T. Guo, D. Ranucci, E. Picco and P.M. Strocchi, High Temperature Alloys for Gas Turbines, (1982) 805–819.
[24] D. Curry and J. Knott, Met. Sci., 13 (1979) 341–345.
[25] G.S. Mahobia, R.G. Sudhakar, A. Antony, K. Chattopadhyay, N.C.S. Srinivas and V. Singh, Proc. Eng., 55 (2013) 830–834.
[26] P. Elliot, C.J. Tyreman and R. Prescott, J. Met., 37 (1985) 20.